Journal of *Marine Science and Engineering*

MDPI

Article

Mechanical Behavior and Sealing Performance Study of Subsea Connector Core-Sealing Components under the Combined Action of Internal Pressure, Bending Moment, and Axial Load

Xiaoquan Hao [1], Feihong Yun [1,*], Kefeng Jiao [1], Xi Chen [2], Peng Jia [1], Xiangyu Wang [1] and Liquan Wang [1]

[1] College of Mechanical and Electrical Engineering, Harbin Engineering University, Harbin 150001, China; haoxiaoquan@hrbeu.edu.cn (X.H.); jiaokefeng@hrbeu.edu.cn (K.J.); jiapeng@hrbeu.edu.cn (P.J.); wangxiangyu@hrbeu.edu.cn (X.W.); wangliquan@hrbeu.edu.cn (L.W.)

[2] College of Mechanical and Electrical Engineering, Heilongjiang Institute of Technology, Harbin 150050, China; chenxi_1113652@hrbeu.edu.cn

* Correspondence: yunfeihong@hrbeu.edu.cn; Tel.: +86-159-4568-3623

Abstract: A complete subsea production system (SPS) is assembled by interconnecting subsea manufacturing facilities through subsea connectors. To ensure the reliability and longevity of the SPS, it is imperative to thoroughly investigate the mechanical behavior and sealing performance of the subsea connector's core-sealing components. In this study, the loading conditions of the subsea clamp connector are examined to analyze the load transfer relationship between its components under different modes. A mathematical model for the load transfer between locking torque and sealing contact pressure is developed for the preloading mode, and the concept of mechanical transfer efficiency is introduced. Another mathematical model for the load transfer between the locking torque and the design pressure is developed for the operation mode. Furthermore, a three-dimensional full-size finite element model of the subsea clamp connector is established to analyze the effects of complex loads on the mechanical behavior and sealing performance of its core-sealing components. The simulation results indicate that internal pressure loading positively affects the sealing of the subsea connector, and that the stress distribution in the core-sealing components under bending moment loading exhibits significant asymmetric characteristics. Additionally, the superposition of axial tensile loads reduces the effect of the bending moment on the strength of the core seal member but further weakens the seal. Finally, an experimental system is designed to validate the simulation results.

Keywords: subsea clamp connector; core-sealing components; load transfer; mechanical behavior; sealing performance

Citation: Hao, X.; Yun, F.; Jiao, K.; Chen, X.; Jia, P.; Wang, X.; Wang, L. Mechanical Behavior and Sealing Performance Study of Subsea Connector Core-Sealing Components under the Combined Action of Internal Pressure, Bending Moment, and Axial Load. *J. Mar. Sci. Eng.* **2023**, *11*, 1691. https://doi.org/10.3390/jmse11091691

Academic Editors: Weicheng Cui, Lian Lian and Dahai Zhang

Received: 7 August 2023
Revised: 24 August 2023
Accepted: 25 August 2023
Published: 27 August 2023

1. Introduction

The subsea production system has emerged as one of the primary methods for developing oil and gas resources in deepwater regions, and is continuously advancing towards ultra-deepwater with higher production equipment demands. The subsea production system consists of essential equipment, including Christmas trees, jumpers, wellheads, pipe manifolds, and others [1]. These components are constructed onshore and installed at designated locations on the seafloor and then connected via subsea connectors to form a complete subsea production system. During operation, the subsea connectors are exposed to high temperature and pressure, as well as internal and external loads from connected equipment and ocean currents [2]. The installation of subsea production systems in deep and ultra-deepwater environments presents complex terrain and operational challenges. Any leakage or failure of subsea connectors under load can lead to substantial repair costs and irreversible damage to the marine environment.

Scholars have extensively researched the sealing performance and design optimization of subsea connectors' core-sealing components, namely, the hub and sealing gasket. For instance, Cascales et al. [3] proposed a mathematical model equivalent to the Murray and Stuart model, which led to an approximate formula for evaluating hub rotation. Dekker et al. [4] developed a design method for pipe clamp connector connections, which had a more reasonable design pressure. Abid et al. [5] showed that bolted flange connectors sealing performance was related to both internal pressure and transient thermal loads. Murali Krishna et al. [6] analyzed the loading and unloading characteristics of a bolted flange joint experimentally and examined the effect of contact stress distribution on the sealing performance using three-dimensional finite element analysis. Takagi et al. [7] predicted the leakage amount by analyzing the spiral wound gasket contact stress distribution and the stress in the hub using the three-dimensional elasto-plastic finite element method. Wang et al. [8] used experimental and finite element methods to study the bending behavior of flange connections under pure bending action, revealing the distribution of contact pressure at the connection end plates. Abid et al. [9] investigated the strength of the hub structure of a non-gasketed bolt flange joint under the combined effect of internal pressure, axial and bending loading, and the sealing capacity of the gasket with different taper angles. Peng et al. [10] optimized and analyzed the mathematical model of the locking mechanism of the subsea clamp connector and established the mathematical model of the force transfer of the subsea clamp connector, which was verified by the finite element method. Nelson et al. [11] proposed an empirical relationship equation for bolt preload that guarantees minimum compressive stress after comparing the sealing performance of single and twin gasket and studying the contact pressure of single and twin gasketed flange joint under bolt preload and internal pressure. Yun et al. [12] established a mathematical model of metal seal contact stress and verified it by finite element analysis and experimental studies. Zhang et al. [13], based on the Hertzian contact theory, derived the analytical equation for the compression of the collector connector and proposed the compression limit equation. Chen et al. [14] analyzed the stress distribution characteristics of the main sealing components of the threaded connector by establishing a three-dimensional elasto-plastic finite element model based on the sealing mechanism of the taper-to-arc seal. Wang et al. [15] established the critical conditions of the sealing performance of the new submarine pipeline mechanical connector and the calculation formula of the sealing contact pressure by analyzing the mechanism of the metal static seal of the connector. Li et al. [16] analyzed the mechanical properties of metal seals of subsea wellhead connectors under preloading and operating mode and determined the theoretical relationship between contact stress and metal seal structural parameters and operating pressure. Liu et al. [17] experimentally investigated the mechanical properties of square steel pipe column joints with bolted flange connections (without sealing role) under combined tensile, bending, and shear loads. Liu et al. [18] developed a new fractal porous media model to analyze the leakage principle of the metal seals of subsea connectors and calculated the permeability of the seal components based on this media model and the length-dependent mechanical model. Duan et al. [19] proposed a stress analysis method (SAM) to solve the theoretical design problem of the main parameters of the hub structure of the subsea connector by establishing a deformation continuum relationship between a thick-walled cylinder and a hollow ring plate. Li et al. [20] theoretically analyzed the load-carrying capacity of subsea wellhead connectors when subjected to external pressure and the bending moment under different operating modes and loading conditions. Yun et al. [21] developed a heat transfer model to investigate the sealing capability of lens-type sealing structures of subsea clamp connectors under the influence of external seawater and internal oil and gas temperature loads. Meanwhile, Zhang et al. [22] proposed an analytical calculation method (ACM) to evaluate the thermal-structural coupling strength and sealing performance of subsea wellhead connectors. Li et al. [23] derived the radial temperature distribution function of a subsea wellhead connection and investigated the effects of internal pressure and temperature on its metal sealing capacity through experimental studies.

The findings from these studies are crucial for improving the reliability and safety of subsea wellhead connectors and advancing the subsea oil and gas industry.

Many previous studies have concentrated on the analysis of the metal seal contact of subsea connectors. These studies have utilized various methods, including theoretical approaches, finite element methods, and experimental methods to investigate the microscopic contact mechanism of the sealing surface, the effect of contact stress, and related parameters such as contact surface width and deformation, as well as the effect of temperature and load on the seal. However, after the subsea connector is connected, it is exposed to a combination of internal oil and gas pressure and external loads (axial and moment loads), which can impact the sealing performance and mechanical behavior of the core-sealing components of the subsea connector. Regarding the investigation into the impact of external loads, the primary focal points encompass diverse connector types, including the gasketless bolted flange connector (primarily serving a connection role), bolted flange connector, subsea collet connector, and subsea wellhead connector. Notably, the subsea clamp connector, as designed within this paper, has yet to be a subject of such research. Amidst the scrutinized connectors, the emphasis has primarily been on exploring the influence of internal pressure or axial tension loads on the connector's sealing function under external loading. However, there has been a notable absence of research regarding the sealing and strength characteristics when the connector is subjected to the combined effect of internal pressure, axial tension, and bending loads.

In this paper, we investigate the sealing and strength performance of the subsea clamp connector under complex loads. Firstly, we analyze the load transfer relationship between each structure under preloading and operation modes, and establish a mathematical model accordingly. Secondly, we develop a simulation model for the core-sealing component of a six-inch subsea connector and conduct finite element analysis to investigate its sealing and strength performance under the combined effects of internal pressure, bending moment load, and axial load. Lastly, we compare the experimental results with the finite element analysis results to validate the accuracy of our mathematical model and finite element simulation.

2. Subsea Connector Structure and Working Principle

The subsea connector structure examined in this study, depicted in Figure 1, is suitable for deployment in shallow water and deep-water environments, and can be installed automatically through ROV-assisted means. The connector is a horizontally operating clamp-type connector, comprising a core structure that primarily consists of a mobile hub, fixed hub, metal sealing gasket with lens-type structure, tightened bolt, and clamp. The fixed hub is welded to the subsea pipe and pre-positioned on the subsea production facility, while the mobile hub is typically welded to both ends of the jumper. The jumper and mobile end are placed together at the designated subsea location and connected to the fixed hub on both sides, forming a complete subsea connection.

In this study, Figure 2a illustrates the state of the subsea connector before locking, while Figure 2b depicts the state after locking. The connector operates by rotating the tensioning bolt using an ROV-operated torque spanner. This action causes the clamp to move radially and hold the mobile and fixed hubs, which creates contact between the tapered hub surface and the spherical surface of the metal lens type sealing gasket, leading to the formation of a seal. The load transfer mechanism in this structure involves multiple components, including the tightened bolt, clamp, hub, and sealing gasket, among others. Due to the complexity and non-uniformity of the load transfer process, it is essential to investigate the load transfer in this structure. Moreover, the subsea connector is exposed to both internal oil and gas pressure from the pipeline and external loads, which can further impact the mechanical properties of the core structure.

Figure 1. Practical application for the subsea connector.

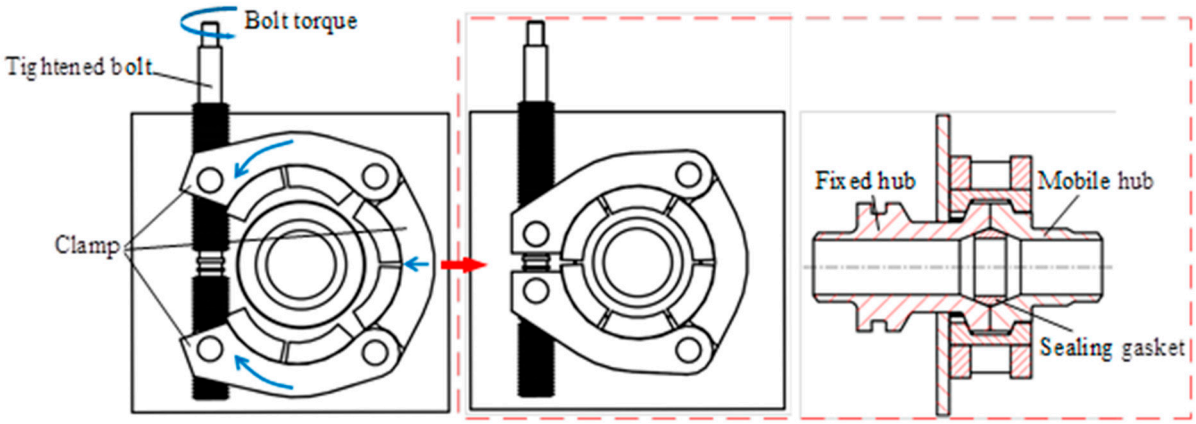

Figure 2. Subsea connector working principle: (**a**) before locking; (**b**) after locking; and (**c**) cross-section.

3. Study of Subsea Connector Load Transfer under Different Work Modes

This paper investigates two working modes of the subsea connector: preloading mode and operating mode. In preloading mode, the metal seal achieves pipe sealing by being subjected to pressure on both sides of the moving end flange and fixed end flange. In operating mode, the connector is subjected to both internal oil and gas pressure and external loads, resulting in a force state that is different from the preload.

The transfer of loads from the bolt to the clamp remains consistent in both modes, therefore, it is analyzed first. Subsequently, the force transfer from the clamp to the metal sealing gasket is analyzed separately in each mode.

3.1. Analysis of Bolt to Clamp Force Transfer

The model of the subsea connector is simplified, as shown in Figure 3. The clamps are simplified to hinges in the model for calculation, with pin 1 between clamp A and clamp B, and pin 2 between clamp B and C. Clamp A and C are connected with pins 3 and 4, respectively, and pins 3 and 4 are connected closer by the tightened bolt.

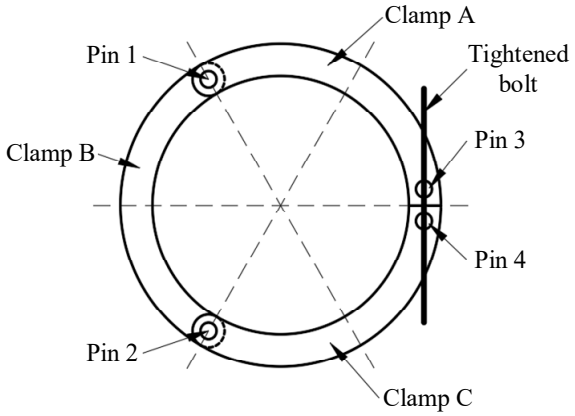

Figure 3. Simplified model of the clamp.

A force analysis of the connection between the tightened bolt and the pin 3 is carried out to obtain the load transfer relationship between the tightening torque T_1 of the approach bolt and the tension F_1 of the pin 3 on the clamp A.

$$T = 2F_1 \cdot \tan(\omega + \rho_v)\frac{d_2}{2} \tag{1}$$

where ρ_v is the equivalent friction angle of the bolt thread, $\rho_v = \tan^{-1}(\mu_1/\cos\lambda)$, λ is the inter-thread friction coefficient. ω is the lead angle, $\omega = \tan^{-1}(p/\pi d_2)$, p is the pitch, and d_2 is the pitch diameter of thread.

3.2. Analysis of Force Transfer from Clamp to Sealing Gasket under Preloading Mode

The hub is acted upon by three clamps uniformly distributed at 120° intervals through the tightened bolt, and Figure 4 illustrates the forces exerted by the tightened bolt on the clamps and by the hub on the clamps. The assumptions made in this analysis are as follows: (1) the linear contact normal force f_{n1}, f_{n2} of the clamp is uniformly distributed around the circumference of the clamp, (2) the loads are in a state of equilibrium after the clamp connection is completed, and (3) the loads are transferred within the annular contact area between the clamp and the flange, and the clamp contact diameter ϕ_{c1} is the average of the flange outer diameter ϕ_0 and the effective inner diameter ϕ_i. Firstly, the analysis of the clamp without considering the frictional action is carried out.

$$\begin{gathered} |F_1| = |F_2| = |F_3| = |F_4| = |F_5| = |F_6| \\ |f_{n1}| = |f_{n2}| \\ \phi_{c1} = (\phi_0 + \phi_i)/2 \end{gathered} \tag{2}$$

where F_2 is the force of pin 3 on clamp A, F_3, F_4 is the force of pin 1 on clamp A and B, respectively, and F_5, F_6 is the force of pin 2 on clamp B and C, respectively. f_{n1} can be decomposed into the line contact radial force f_{r1} and axial force f_{a1} of the fixed hub on the clamp, and similarly, f_{n2} can be decomposed into the line contact radial force f_{r2} and axial force f_{a2} of the mobile hub on the clamp.

The frictional action existing between the clamps and the hub under preloading conditions is analyzed. As the stiffness of the clamps is significant and they do not move completely radially with respect to the flange, it is reasonable to assume that no deformation will occur. After the connector is connected, each clamp tends to move closer to the center, and the frictional force acting on the clamp is opposite to its tendency to move inward. Figure 5 illustrates the movement of clamp A, which tends to rotate 30° clockwise inward along the y-axis. Consequently, the direction of friction in the shaft section is 30° clockwise outward along the y-axis. Similarly, the direction of friction in clamp B is outward along

the x-axis, while the direction of friction in clamp C is 30° counterclockwise outward in the negative direction of the y-axis.

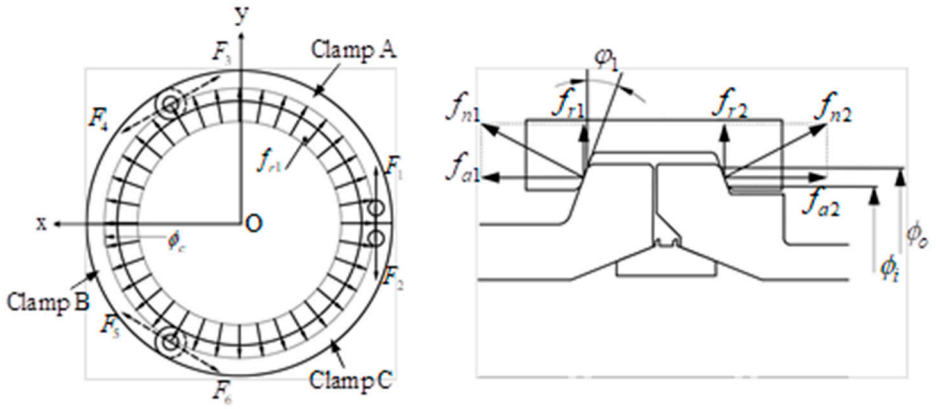

Figure 4. Force analysis of clamps: (**a**) radial force analysis of clamps and (**b**) force analysis of clamp shaft sections.

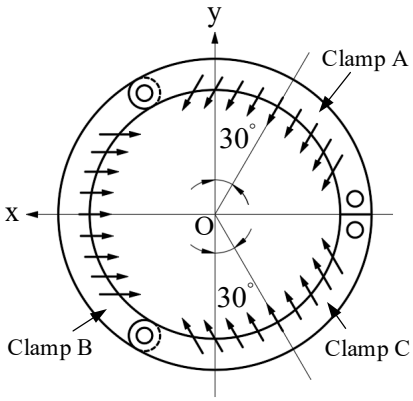

Figure 5. Clamp movement trend.

As the three clamps are equally distributed around the hub with a center angle of 120° and exert the same magnitude of force, differing only in direction, we will focus on the mechanical analysis of clamp B below. Figure 6 shows that the angle β between the contact segment area and the clamp along the x-axis is a function of the circumferential position and is expressed as an angle α. For calculation convenience, the angle range for α is chosen to be 30° to 150°.

$$\tan\beta = \tan\varphi \sin\alpha (30^\circ \le \alpha \le 150^\circ) \tag{3}$$

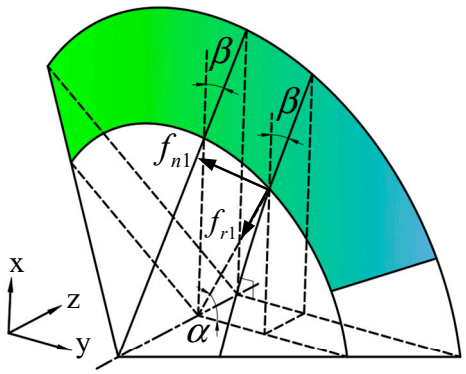

Figure 6. Clamp B contact area with hub.

The equilibrium equation is established in the x-axis direction of clamp B. $f_{r1}\sin\alpha$ is used as the component of f_{n1} along the x-axis, and $\mu_2 f_{n1}\cos\beta$ is used as the friction force along the x-axis, where μ_2 is the friction coefficient.

$$\int_{\pi/6}^{5\pi/6}(f_{r1}\sin\alpha+\mu_2 f_{n1}\cos\beta)\frac{\phi_{c1}}{2}d\alpha=F_6\cos\frac{\pi}{6} \tag{4}$$

Combining Equation (2) with (4) and using $f_{a1}=f_{n1}\cos\varphi_1=f_{r1}/\tan\varphi_1$, we obtain the following:

$$f_{a1}=\frac{9\sqrt{3}F_1\sqrt{4+\tan^2\varphi_1}\sqrt{4+3\ \tan^2\varphi_1}}{9\sqrt{3}\phi_{c1}\sin\varphi_1\sqrt{4+\tan^2\varphi_1}\sqrt{4+3\ \tan^2\varphi_1}+\pi\mu_2\phi_{c1}(4\sqrt{4+3\ \tan^2\varphi_1}+2\sqrt{4+\tan^2\varphi_1})} \tag{5}$$

Denoting $\sqrt{4+\tan^2\varphi_1}$ as ψ_1 and $\sqrt{4+3\ \tan^2\varphi_1}$ as ψ_2, the above equation can be simplified as follows:

$$f_{a1}=\frac{9\sqrt{3}F_1\psi_1\psi_2}{9\sqrt{3}\phi_{c1}\sin\varphi_1\psi_1\psi_2+\pi\mu_2\phi_{c1}(4\psi_2+2\psi_1)} \tag{6}$$

The total axial frictional force component ΔF_{a1} resulting from friction is analyzed. Integrating the axial friction component $\mu_2 f_{n1}\sin\beta$ in the range of angle α 30° to 90° creates the effect of 1/6 of the frictional force due to friction in the axial direction, and the total axial force due to friction is six times the value of this integral.

$$\Delta F_{a1}=6\int_{\pi/6}^{\pi/2}\mu_2 f_{n1}\sin\beta\frac{\phi_{c1}}{2}d\alpha=\frac{27\sqrt{3}\mu_2F_1\psi_1\psi_2[\pi-2\arctan(\frac{\sqrt{5+3\cos2\varphi_1}}{\sqrt{6}\sin2\varphi_1})]}{9\sqrt{3}\sin2\varphi_1\psi_1\psi_2+2\pi\mu_2\cos\varphi_1(4\psi_2+2\psi_1)} \tag{7}$$

Calculation and analysis of Equation (7) under preloading mode: The axial friction generated by the friction has a negative effect on the clamp under preloading mode. Therefore, the total axial force F_{A1} exerted by the hub on the clamp under preloading mode is given by the following:

$$F_{A1}=\pi\phi_{c1}f_{a1}-\Delta F_{a1}=\frac{18\sqrt{3}\pi F_1\cos\varphi_1\psi_1\psi_2-27\sqrt{3}\mu_2F_1\psi_1\psi_2[\pi-2\arctan(\frac{\sqrt{5+3\cos2\varphi_1}}{\sqrt{6}\sin2\varphi_1})]}{9\sqrt{3}\sin2\varphi_1\psi_1\psi_2+2\pi\mu_2\cos\varphi_1(4\psi_2+2\psi_1)} \tag{8}$$

The force analysis of the mobile hub and the fixed hub is shown in Figure 7, where ϕ_{c2} is the contact diameter of the hub in contact with the metal sealing gasket. The reaction force f_{T3}, f_{T4} of the clamp B acts on its contact area with the hub, and the reaction force of the metal sealing gasket acts on its contact area with the hub with a horizontal reaction force of f_{A5}, f_{A6}, $f_{A5}=-f_{A6}$. The total axial force F_{A3} of the clamp on the hub and the total axial force F_{A5}, F_{A6} of the metal sealing gasket on the hub are equal in magnitude. Assume that the forces between the hub and the sealing gasket are uniformly distributed.

$$F_{A1}=F_{A3}=\pi\phi_{c2}f_{A5} \tag{9}$$

A force analysis is conducted on the metal sealing gasket, as depicted in Figure 8. The seal contact area experiences hub compression and friction. Under preloading conditions, the hub has a tendency to move outward with respect to the metal sealing gasket axis. The metal sealing gasket experiences tangential frictional forces from the fixed and mobile hubs, denoted as f_{f1} and f_{f2}, respectively, acting outward relative to the metal sealing gasket axis. The contact pressures are f_{N1}, f_{N2}, and $|f_{N1}|=|f_{N2}|$.

$$f_{A5}=f_{A7}=f_{T7}\cos(\varphi_2-\gamma)=\frac{f_{n1}}{\cos\gamma}\cos(\varphi_2-\gamma) \tag{10}$$

where f_{T7} is the combined force of the contact pressure f_{N1} and friction force f_{f1} between the fixed hub and the sealing gasket, γ is the friction angle of the contact surface of the metal sealing gasket, φ_2 is the inclination angle of the contact surface of the hub and the metal sealing gasket, f_{A7} is the horizontal extrusion force, namely, locking force or preload, and the horizontal component of resultant force f_{T7}, $|f_{A7}| = |f_{A8}|$.

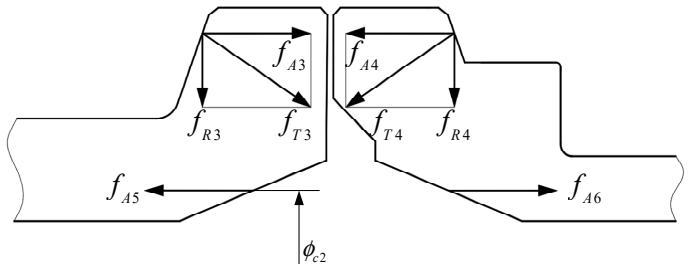

Figure 7. Flange force analysis.

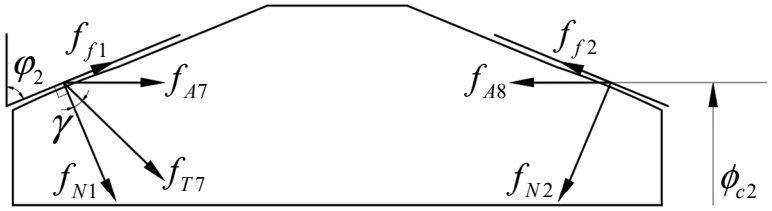

Figure 8. Force analysis of metal sealing gasket.

The relationship between the contact pressure f_{N1} of the metal sealing gasket and the torque T of the tightened bolt can be obtained by combining (1), (8), (9), and (10):

$$f_{N1} = \frac{18\sqrt{3}\pi\cos\varphi_1\cos\gamma\psi_1\psi_2 - 27\sqrt{3}\mu_2\cos\gamma\psi_1\psi_2[\pi - 2\arctan(\frac{\sqrt{5+3\cos 2\varphi_1}}{\sqrt{6}\sin 2\varphi_1})]}{2\pi d_2\phi_{c2}\tan(\omega+\rho_v)\cos\varphi_1\cos(\varphi_2-\gamma)[9\sqrt{3}\sin\varphi_1\psi_1\psi_2 + \pi\mu_2(4\psi_2+2\psi_1)]}T \quad (11)$$

Equation (11) shows the relationship between the tightened torque of the subsea connector and the average contact pressure generated in the contact area of the sealing gasket under preloading conditions. The magnitude of the contact pressure f_{N1} is related to the structural parameters and deformation of the metal sealing gasket, which is one of the factors determining the sealing performance, and another determining factor is the contact width of the sealing area [13,24].

$$\eta = \frac{T}{f_{N1}} = \frac{2\pi d_2\phi_{c2}\tan(\omega+\rho_v)\cos\varphi_1\cos(\varphi_2-\gamma)[9\sqrt{3}\sin\varphi_1\psi_1\psi_2 + \pi\mu_2(4\psi_2+2\psi_1)]}{18\sqrt{3}\pi\cos\varphi_1\cos\gamma\psi_1\psi_2 - 27\sqrt{3}\mu_2\cos\gamma\psi_1\psi_2[\pi - 2\arctan(\frac{\sqrt{5+3\cos 2\varphi_1}}{\sqrt{6}\sin 2\varphi_1})]} \quad (12)$$

η can be defined as the connector mechanical transfer efficiency, which reflects the connector locking mechanism force transfer performance.

3.3. Analysis of Force Transfer from Clamp to Sealing Gasket under Operation Mode

The analysis investigates the frictional forces between the clamp and the hub during operation mode, as illustrated in Figure 9. When subjected to internal oil and gas pressure, the clamp A tends to rotate outward by 30° clockwise along the y-axis, resulting in a

friction direction of clamp A that is 30° clockwise inward along the y-axis in the shaft section. Similarly, clamp B tends to rotate outward along the x-axis, which creates a friction direction of clamp B that is inward along the x-axis in the shaft section. The movement of clamp C tends to rotate 30° counterclockwise outward along the negative direction of the y-axis, so the direction of friction in the shaft section is 30° counterclockwise in the negative direction of the y-axis. Likewise, the tendency of clamp C is to rotate 30° outward counterclockwise along the negative direction of y-axis, resulting in a friction direction that is 30° inward counterclockwise in the negative direction of the y-axis in the shaft section.

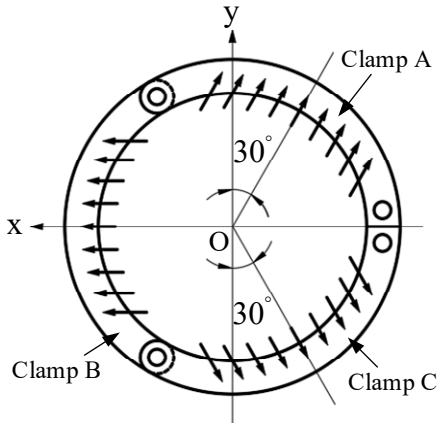

Figure 9. Trend in clamp movement.

As the forces of the three clamps have the same magnitude and distribution, only the directional differences require separate analysis. For simplicity, the force analysis in this study is conducted only for clamp B. To differentiate the forces under preloading and operation modes, all forces under operation mode are denoted with a prime symbol "′".

Establish the equilibrium equation in the x-axis direction of the clamp B, $f_{r1}{}' \sin\alpha$ as the component of $f_{n1}{}'$ along the x-axis and $\mu_2 f_{n1}{}' \cos\beta$ as the frictional force along the x-axis, where μ_2 is the friction coefficient.

$$\int_{\pi/6}^{5\pi/6} \left(f_{r1}{}' \sin\alpha - \mu_2 f_{n1}{}' \cos\beta\right) \frac{\phi_{c1}}{2} d\alpha = F_6 \cos\frac{\pi}{6} \tag{13}$$

Combining Equation (2) with (13) and using $f_{a1}{}' = f_{n1}{}' \cos\varphi_1 = f_{r1}{}' / \tan\varphi_1$, we obtain the following:

$$f_{a1}{}' = \frac{9\sqrt{3} F_1 \psi_1 \psi_2}{9\sqrt{3}\phi_{c1} \sin\varphi_1 \psi_1 \psi_2 - \pi\mu_2 \phi_{c1}(4\psi_2 + 2\psi_1)} \tag{14}$$

The total axial frictional component $\Delta F_{a1}{}'$ due to friction is analyzed. By integrating the axial friction component $\mu f_{n1}{}' \sin\beta$ over the range of angle α 30° to 90°, the effect of 1/6 of the frictional force in the axial direction due to friction is obtained.

$$\Delta F_{a1}{}' = 6\int_{\pi/6}^{\pi/2} \mu_2 f_{n1}{}' \sin\beta \frac{\phi_{c1}}{2} d\alpha = \frac{27\sqrt{3}\mu_2 F_1 \psi_1 \psi_2 [\pi - 2\arctan(\frac{\sqrt{5+3\cos 2\varphi_1}}{\sqrt{6}\sin 2\varphi_1})]}{9\sqrt{3}\sin 2\varphi_1 \psi_1 \psi_2 + 2\pi\mu_2 \cos\varphi_1 (4\psi_2 + 2\psi_1)} \tag{15}$$

In the operation mode, the hub tends to compress and separate the clamp due to the pressure of oil and gas inside the pipe. At this time, the axial component of the friction force exerts a positive effect on the clamp. Thus, the total axial force $F_{A1}{}'$ generated on the clamp under the operation mode is given by the following:

$$F_{A1}{}' = \pi\phi_{c1} f_{a1}{}' + \Delta F_{a1}{}' \tag{16}$$

Mechanical analysis of the mobile hub and fixed hub, the two are subjected to the same force state, as shown in Figure 10, where $f_{A1}{}' = -f_{A3}{}' = f_{A4}{}'$; f_{ph5}, f_{ph6} is the equivalent horizontal force of the internal pressure p_{in} acting on the hub, and $f_{ph5} = -f_{ph6}$; the reaction force of the clamp B $f_{T3}{}'$, $f_{T4}{}'$ acting on its contact area with the hub; the reaction force of the metal sealing gasket acts on its contact area with the hub, and the horizontal reaction force is $f_{A5}{}'$, $f_{A6}{}'$, and $f_{A5}{}' = -f_{A6}{}'$; ϕ_{c2} is the contact diameter of the hub in contact with the metal sealing gasket. Assume that the forces between the hub and the sealing gasket are uniformly distributed.

$$F_{A1}{}' = F_{A3}{}' = \pi\phi_{c2}(f_{A5}{}' + f_{ph5}) \tag{17}$$

$$f_{ph5} = \frac{\pi{\phi_{c2}}^2}{4} p_{in} \Big/ (\pi\phi_{c2}) = \frac{\phi_{c2}}{4} p_{in} \tag{18}$$

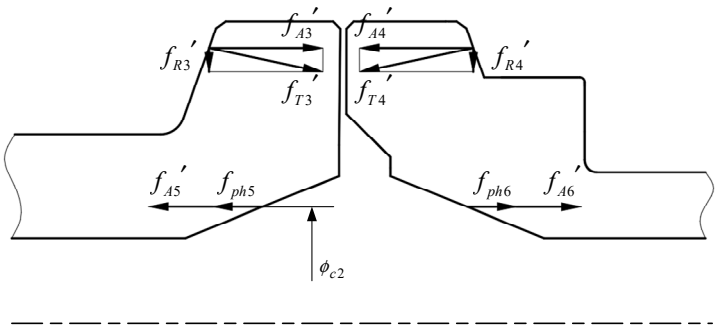

Figure 10. Operation mode hub force analysis.

$f_{A5}{}'$ can also be referred to as the residual preload force under the operation mode [12], which can be expressed as

$$f_{A5}{}' = b\bar{q}\tan(\varphi_2 - \gamma) \tag{19}$$

where, p_{in} is the internal design pressure, which is 34.5 MPa in this study, b is the width of the contact area when the sealing gasket is pressed, $b = 16\bar{q}r/\pi E^*$, r is the radius of the sealing spherical surface of the metal sealing gasket, E^* is related to the material of the two components in contact, the material of the hub in this paper is F22, and the material of the metal sealing gasket is Incoloy 825, so it is $E^* = 1.128 \times 10^5$ MPa, $\bar{q}$ is the average contact pressure of the sealing contact area, $\bar{q} = mp_{in} = 224.5$ MPa under the operation mode, which is the minimum preloading specific pressure, and m is the gasket coefficient, which indicates the ratio of the contact pressure applied on the unit effective area to the internal pressure, and in this paper, the metal seal material is Incoloy 825, so $m = 6.5$ [12].

The relationship between the tightening torque and the design pressure of the subsea connector in the operation mode can be obtained by combining (1), (14)–(19) with a factor of three as a safety margin (employed to withstand external loads):

$$T = \frac{3F_1\left(\pi\phi_{c2}b\bar{q}\tan(\varphi_2 - \gamma) + \frac{\pi{\phi_{c2}}^2}{4}p_{in}\right)\tan(\omega + \rho_v)d_2}{\pi\phi_{c1}f_{a1}{}' + \Delta F_{a1}{}'} \tag{20}$$

4. Finite Element Simulation

In order to investigate the sealing performance and mechanical behavior of the core-sealing components of the subsea clamp connector under loads of internal pressure, tension, and bending moment, a full-size three-dimensional finite element model was employed for finite element simulation analysis. The initial loading conditions used in the simulation study were derived from the analysis presented in Section 1, which served as the foundation for the simulation study.

4.1. Three-Dimensional Finite Element Model

Ansys Workbench is used to simulate the six-inch subsea clamp connector using a complete three-dimensional finite element model. The main parameters of the six-inch subsea clamp connector are shown in Table 1. In this paper, the connector model is simplified to a certain extent, only studying the core components of the connector, such as the mobile hub, fixed hub, and metal sealing gasket. The simplified model is shown in Figure 11, and the six clamps are used only to simulate the role of real loading.

Table 1. Six-inch subsea connector geometry dimensions.

Name of Parameter	Parameter Value	Name of Parameter	Parameter Value
Lead angle ω	1.27°	Clamp inclination angle φ_1	20°
Equivalent friction angle ρ_v	8.83°	Sealing gasket inclination angle φ_2	23°
Pitch diameter of thread d_2	57.402 mm	Thread friction coefficient μ_1	0.15
Clamp contact diameter ϕ_{c1}	295 mm	Friction coefficient between components μ_2	0.15
Seal contact diameter ϕ_{c2}	167 mm	Friction angle of sealing gasket γ	8.53°

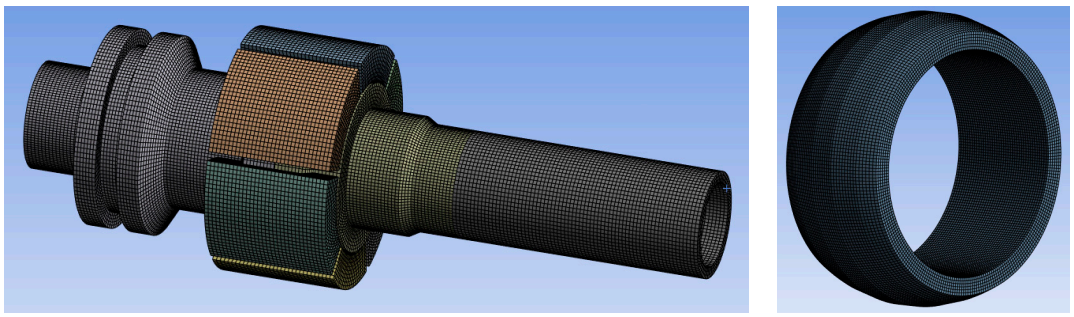

(**a**) (**b**)

Figure 11. Simplified model and meshing: (**a**) simplified model and (**b**) sealing gasket.

For the analysis, Solid 185 elements were utilized to model all parts. The steel-to-steel friction coefficient is set at 0.15, and the model contains a total of 210,636 elements and 257,940 nodes. Hexahedral meshes were employed for all parts, as illustrated in Figure 11.

The material used for the hub and clamp is F22, while the metal sealing gasket is made of Incoloy 825, and the pipe is made of X65, as presented in Table 2. During operation, the metal sealing gasket may undergo plastic deformation at the contact area with the hub, resulting in nonlinear material behavior. Hence, a nonlinear material model, specifically a bilinear isotropic hardening model, was employed for analysis. The material curve for this model is shown in Figure 12.

Table 2. Material properties.

Material	Yield Strength (MPa)	Tensile Strength (MPa)	Poisson Ratio	Density (g/cm^3)	Elastic Modulus (GPa)
X65	450	535	0.3	7.85	207
Incoloy 825	241	586	0.275	8.14	205
F22	552	689	0.286	7.85	211

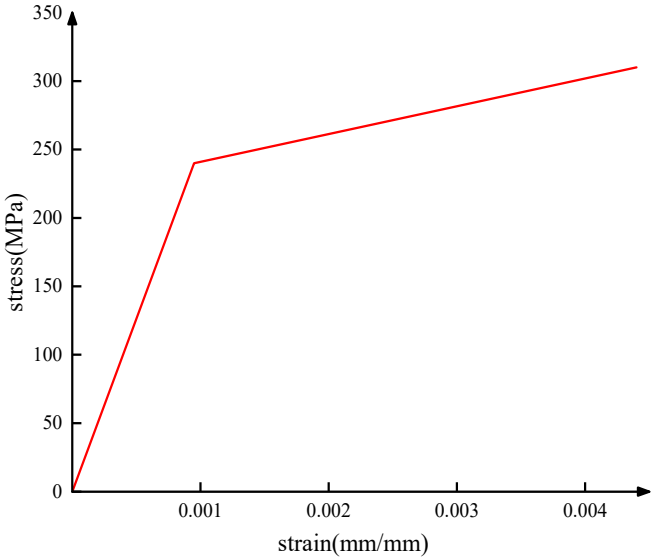

Figure 12. Bilinear isotropic hardening stress–strain curve for Incoloy 825.

To evaluate the performance of the subsea connector, two factors are considered, i.e., connection strength and sealing capacity. The connection strength is evaluated based on the von Mises stress of the hubs and clamps, which must not exceed their yield strength. The von Mises stress of the metal sealing gasket may exceed its yield strength, but must not exceed its tensile strength. Sealing capacity is evaluated based on the average contact pressure and contact width of the metal sealing gasket and hub [25,26].

$$\begin{cases} \overline{q} \geq 6.5 p_{in} = 224.5 \text{ Mpa} \\ b \geq 2 \text{ mm} \end{cases} \tag{21}$$

where connector design pressure p_{in}: 34.5 MPa, and b is the seal contact width.

4.2. Boundary Conditions

The contact surface between the fixed hub and external components is fixed in accordance with the actual working conditions, and internal pressure is applied to the pipe, hub, and metal sealing gasket. An axial load is applied to the end of the pipe, while a bending load is applied at a distance of 821.5 mm from the centerline of the fixed hub, as depicted in Figure 13. The application points of the axial tensile load and bending moment load are distant from the sealing location. The Saint-Venant principle [27] indicates that the impact on the stress distribution in the core-sealing components of the connector can be disregarded.

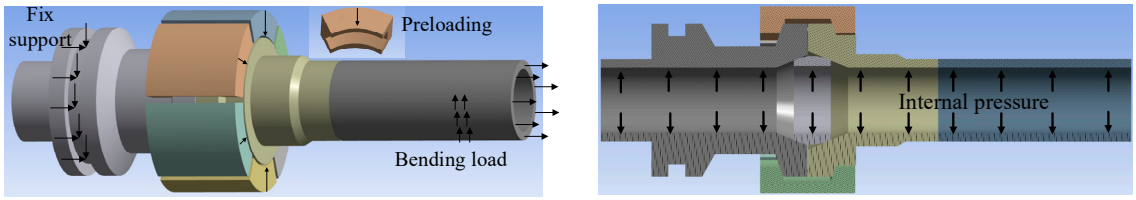

Figure 13. Boundary condition loading: (**a**) axial tensile load and bending moment loading and (**b**) internal pressure loading.

To simulate the loading process of the subsea connector during actual operation, four loading steps have been established. In the first loading step (S_{pre}), by substituting the design pressure of 34.5 MPa into Equation (20), the preload torque is determined to be

1799.39 Nm. After this step is completed, preloading is achieved, and the sealing condition is formed. In the second loading step (S_{in}), 34.5 MPa internal pressure is applied. In the third loading step (S_b), a bending moment of 174 kNm is applied. Finally, in the fourth loading step (S_{ax}), an axial tensile tension of 212 kN is applied. These loading steps are presented in Table 3.

Table 3. Load loading steps.

Step	Load	The Parameter Value
S_{pre}	Preloading	1799.39 Nm
S_{in}	Internal pressure	34.5 MPa
S_b	Bending moment	174 kNm
S_{ax}	Axial tensile load	212 kN
S_o	Unloading axial tension and bending load	/

To investigate the stress distribution in the core components of the seal, namely, the mobile hub, fixed hub, and sealing gasket, eight paths are established with their definitions, and codes presented in Table 4. Figure 14 depicts the schematic diagram of these paths along with their respective starting points.

Table 4. The definitions and code of critical node paths.

Path Code	The Definition of Path	The Starting Point
P−1	Mobile hub circulation direction	P1
P−2	Mobile hub axial side under compression	P2
P−3	Mobile hub axial side under tension	P3
P−4	Fixed hub circulation direction	P4
P−5	Fixed hub axial side under compression	P5
P−6	Fixed hub axial side under tension	P6
P−7	Connector compression side sealing gasket contact surface	P7 (Near the fixed hub)
P−8	Connector tension side sealing gasket contact surface	P8 (Near the fixed hub)

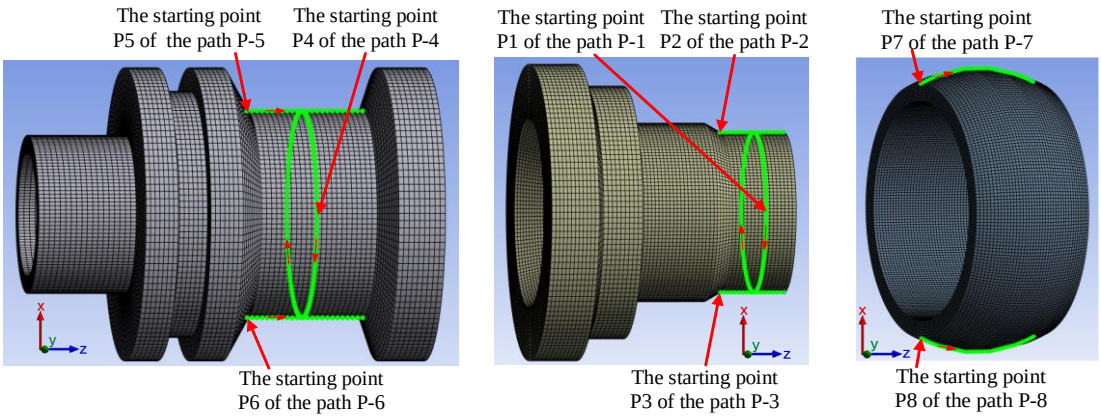

Figure 14. Diagram of the critical path and the corresponding starting point. (**a**) fixed hub; (**b**) mobile hub; and (**c**) sealing gasket.

4.3. Analysis of FE Simulation Results

Figure 15a–d depicts the distribution of von Mises stress for the core-sealing components of the subsea connector under four distinct working conditions.

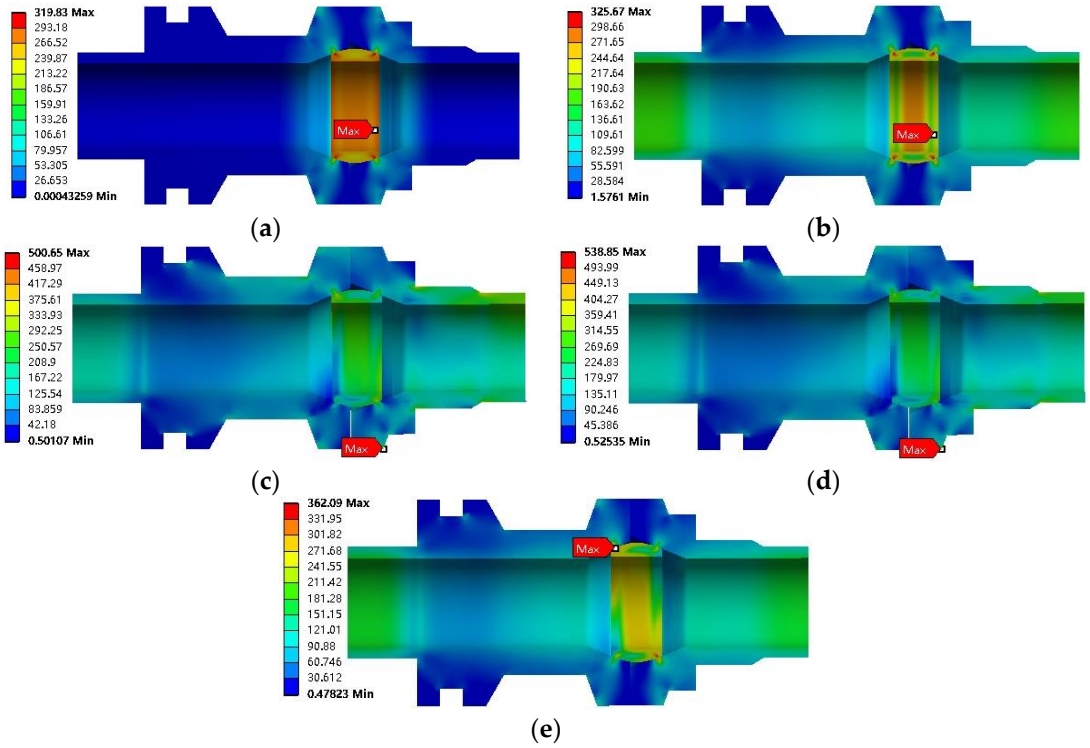

Figure 15. Distribution of von Mises stress under different working conditions: (**a**) S_{pre}; (**b**) S_{in}; (**c**) S_b; (**d**) S_{ax}; and (**e**) S_o.

4.3.1. The Mechanical Properties Analysis on Hub Critical Path

Figure 16a illustrates the stress distribution along the circumferential critical path of the mobile hub. The loading of the S_b condition results in an asymmetric stress distribution in the circumferential position, with the average stress on the compressive side being 61.4 MPa higher than that on the tensile side. This indicates that the superposition of bending moments has a greater effect on the compressive side of the mobile hub circumferential than on its tensile side.

The stress distribution on the axial critical path of the mobile hub is illustrated in Figure 16b. Upon loading the S_b condition, the stresses in the P−2 and P−3 paths gradually decrease, with the maximum and average stresses in the P−2 path being 393.04 MPa and 311.7 MPa, respectively, and the maximum and average stresses in the P−3 path being 317.56 MPa and 229.79 MPa, respectively. This indicates that the superposition of bending moments has a greater effect on the mobile hub near the seal, and the effect on the compressed side is greater than that on the tensile side. Upon loading the S_{ax} condition, the average stress in the P−2 path decreases by 24.36 MPa, while the average stress in the P−3 path increases by 24.47 MPa. This suggests that the superposition of the axial tensile load can attenuate the uneven stress distribution generated by the bending moment for the mobile hub in the axial direction.

The stress distribution on the path of the fixed hub is illustrated in Figure 16c,d. The analysis process is the same as described above, and it leads to the same conclusions. The axial stress of the fixed hub exhibits a distinctly different behavior compared to that of the mobile hub. Specifically, the stress level of the mobile hub exceeds that of the fixed hub following the application of both bending moment and axial tensile load. This suggests that greater emphasis should be placed on the design of the mobile hub during structural engineering endeavors.

Hub maximum rotation when bending moment load is applied is shown in Figure 17. The maximum rotation angle of the hubs appears on the tension side and increases with

the increase in bending moment. The maximum rotation angle generated between the hubs is 1.43°. The influence on seals is analyzed in the following section.

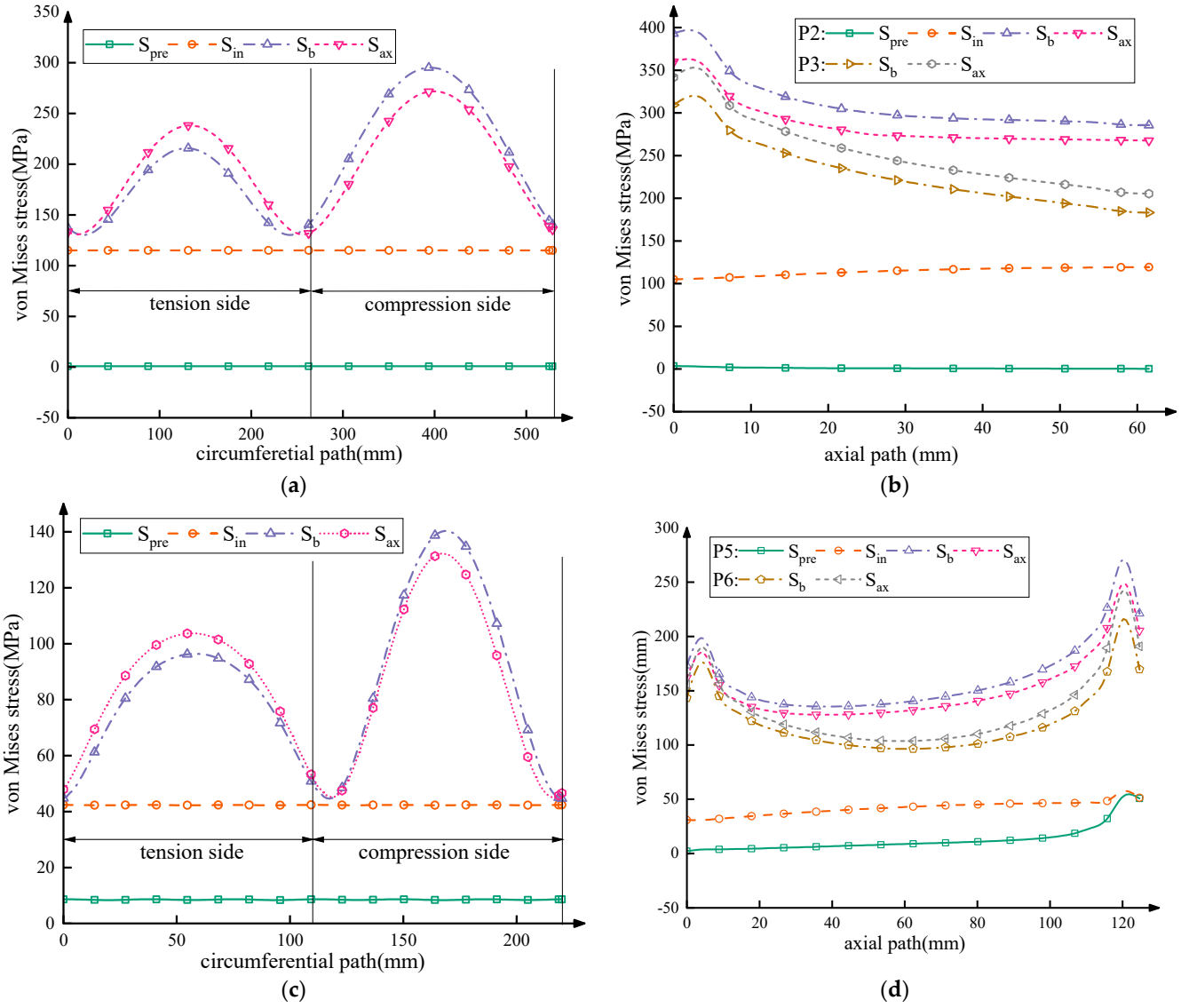

Figure 16. Critical path von Mises stress distribution: (**a**) P−1; (**b**) P−2, P−3; (**c**) P−4; and (**d**) P−5, P−6.

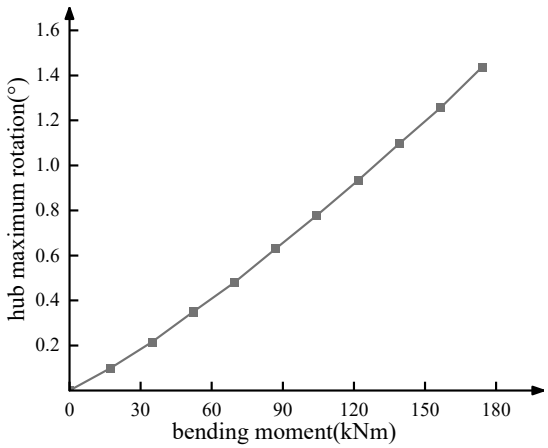

Figure 17. Hub maximum rotation.

4.3.2. Mechanical Properties Analysis of the Metal Seal

The stress distribution on the critical path of the metal seal is depicted in Figure 18a. Under the S_b loading condition, the stress on the compressive side of the metal sealing gasket increases along the P−7 path, reaching a maximum increase of 12.54 MPa, while the stress on the tensile side decreases with a maximum decrease of 30.69 MPa. Similarly, the stress on the tensile side of the P−8 path also experiences a decrease, with a maximum decrease of 52.25 MPa, whereas the stress on the compressive side increases, reaching a maximum increase of 23.58 MPa. Notably, the tensile side of the contact position with the fixed hub bears the greatest impact of the bending moment. Under the S_o loading condition, the stresses on the pressurized side of the P−7 and P−8 paths increase further due to plastic strain generation.

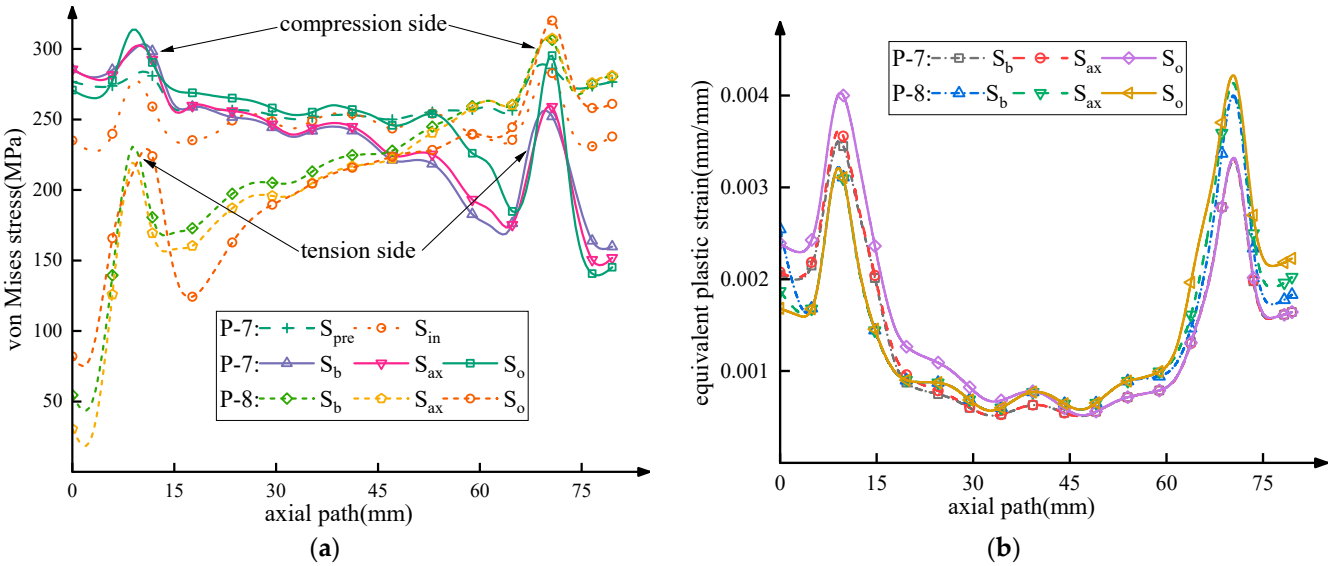

Figure 18. (**a**) Von Mises stress distribution. (**b**) Equivalent plastic strain.

The equivalent plastic strains on the critical paths of the seals are shown in Figure 18b. After loading the S_b condition, there are obvious plastic strains on the pressurized side of the P−7 and P−8 paths, and the maximum equivalent strains are 0.00335 and 0.00397, respectively. After loading the S_{ax} condition, the distributions of plastic strains on the P−7 and P−8 paths are basically the same as that of the Sb condition. After loading the S_o condition, the plastic strain on the pressurized side of the P−7 path and the P−8 path increases further, which is due to the fact that after releasing the external load, the seals are equivalent to carrying out the loading action.

4.3.3. The Contact Properties Analysis of the Metal Seal

The contact pressure of the metal sealing gasket is shown in Figure 19, and the contact pressure in the seal contact area is parabolic in distribution regardless of the working conditions, which is consistent with the sealing mechanism of the metal sealing cone to arc surface [14]. The average contact pressure and seal contact width in the seal contact area are shown in Table 5. Upon loading the S_b condition, the contact pressure and contact width of the metal sealing gasket on the tensile side are reduced compared to the results observed under preload conditions, particularly on the tensile side of the P−7 path, where they decrease to 260.08 MPa and 3.8 mm, respectively. This suggests that the superposition of bending moment has a significant impact on the seal, especially on the tensile side of the sealing gasket. Upon loading the S_{ax} condition, the contact pressure and seal width of the metal sealing gasket on the tensile side further decrease, particularly on the tensile side of the P−8 path, where they decrease to 240.25 MPa and 2.7 mm, respectively, approaching critical sealing conditions. This indicates that the superposition of axial tensile load further

reduces the reliability of the subsea connector seal. After loading the S_o condition, which releases the effects of loads unfavorable to the seal, the seal contact pressure and contact zone width increase. Although the external loads are all axisymmetric, the seal contact pressure has become less symmetric due to the appearance of plastic deformation.

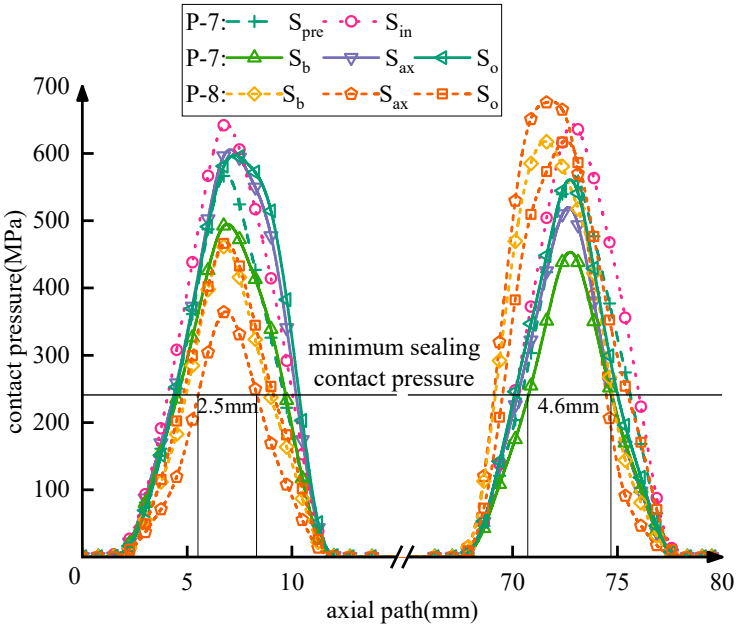

Figure 19. Contract pressure of the metal seal.

Table 5. The seal characteristic of sealing surface.

Work Condition	S_{pre}	S_{in}	S_b (P−7)	S_b (P−8)	S_{ax} (P−7)	S_{ax} (P−8)	S_o (P−7)	S_o (P−8)
average contact pressure (close to the fixed hub, MPa)	340.17	407.70	318.08	262.75	395.16	240.25	401.23	268.35
average contact pressure (close to the mobile hub, MPa)	340.17	407.70	260.08	417.55	297.02	409.53	310.74	421.64
seal band width (close to the fixed hub, mm)	5.1	5.8	5.0	4.0	5.7	2.7	5.7	4.2
seal band width (close to the mobile hub, mm)	5.1	5.8	3.8	5.4	3.5	5.3	3.7	4.9

In summary, the core-sealing components of the six-inch subsea connector form the seal under the action of preload. The superposition of internal pressure, bending moment, and axial force has an adverse effect on its strength, especially for the metal sealing gasket. These loads cause a certain degree of plastic deformation in the contact area but do not lead to destructive failure. Although the seal contact surface after load superposition is close to the minimum sealing requirements, no seal failure occurs.

5. Experimental Study

To investigate the mechanical behavior of the core-sealing components of the subsea connector under external loads and their effect on the sealing performance, an equivalent sealing experimental system was designed. The experimental results were then compared with the finite element results for validation.

5.1. Experimental System

5.1.1. Experimental Equipment

Figure 20 showed the schematic diagram of the experiment that loaded the subsea connector with internal pressure and bending moment load. The experimental equipment consisted of a subsea connector, a bending moment test facility, a hydraulic pump for generating internal fluid pressure, a hydraulic station for applying bending moment, a torque wrench, a sensor with 0.1 MPa accuracy, a static strain system, and strain gauges. The Class 4 torque wrench provided the 1799.39 Nm torque required for the initial seal, which was consistent with the value loaded analytically during the finite element simulation.

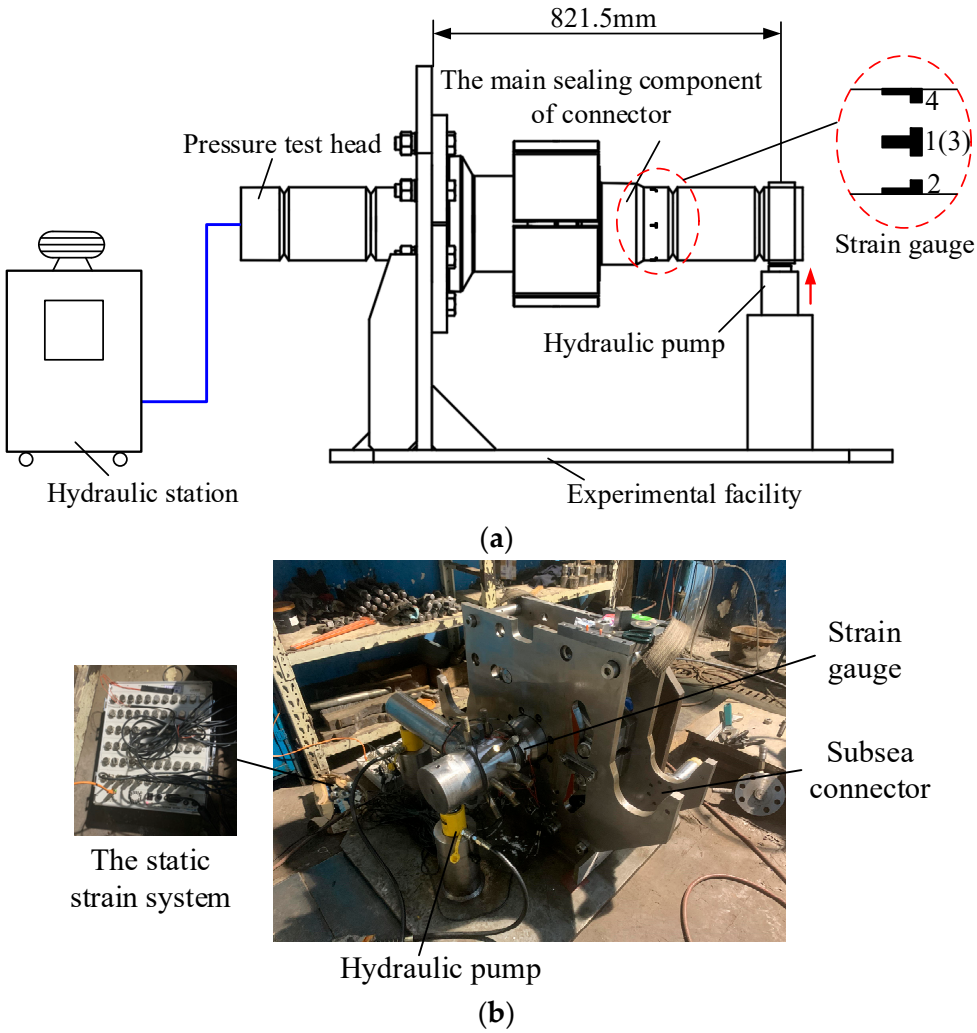

Figure 20. Schematic diagram of external load loading experiment: (**a**) schematic diagram of the experimental program and (**b**) experimental equipment.

Eight strain gauges of the same type were positioned as depicted in Figure 20a. Four sets of strain gauges were arranged at 90° intervals in the circumferential critical position of the movable hub. Each set included one strain gauge in the axial direction and one in the circumferential direction.

5.1.2. Experimental Procedure

The experiment was conducted with loaded internal pressure and moment load, and it was repeated three times to minimize the impact of experimental errors. According to API Spec 6A [28], stable pressure and effective sealing capacity are achieved when the pressure change per hour is not greater than 5% of the experiment or 3.45 MPa/h

(500 psi/h), whichever is smaller, under pressurization, as long as no leakage occurs. The specific experimental procedures are outlined as follows:

1. Filling the hydraulic station with experimental water and starting the pressurization process;
2. Stopping the pressurization process when the pressure sensor reached 100% of the rated working pressure (34.5 MPa), and holding the pressure for 15 min while checking for any leakage in the connector. The pressure data and strain data were recorded after the pressure-holding period;
3. Applying the bending moment up to the theoretical limit (174 kNm) and holding the pressure for 15 min while checking for any leakage in the connector. The pressure data and strain data were recorded after the holding pressure was completed;
4. Unloading the moment and pressure;
5. Repeating the above steps (1)–(4) three times.

5.2. Discussion of Experimental Result

5.2.1. Sealing Capacity Discussion

The pressure change under internal pressure and bending moment loading was shown in Table 6. The experimental results showed that the internal pressure change after internal pressure and bending moment loading was very small, the maximum pressure drop was 0.2 MPa, and the maximum pressure change was 0.57%, which satisfied the sealing requirements, and there was no leakage during the whole experiment, which proved the good sealing performance.

Table 6. Pressure variation condition.

Number of Experiments	Working Condition	Pressure before Pressure-Holding (MPa)	Pressure after Pressure-Holding (MPa)	Decreasing Pressure (MPa)	Pressure Variation (%)
1	Sin	35.0	35.0	0	0
	Sb		34.8	0.2	0.57
2	Sin	35.0	34.8	0.2	0.57
	Sb		34.8	0.2	0.57
3	Sin	34.9	35.0	0	0
	Sb		34.9	0.1	0.29

The pressure variations resulting from internal pressure and bending moment loading were presented in Table 6. The experimental findings demonstrated that the internal pressure changes after the application of internal pressure and bending moment loads were minimal, with a maximum pressure drop of 0.2 MPa and a maximum pressure variation of 0.57%. These changes were within the acceptable range of sealing requirements specified by the API Spec 6A [28]. Furthermore, no leakage was observed during the entire experiment, indicating the excellent sealing performance of the subsea connector.

5.2.2. Strength Performance Discussion

The stress results of three experiments conducted at the location of the strain gauge under preload, internal pressure, and bending moment loading were compared with the simulation results, as presented in Table 7 and Figure 21. The findings are summarized as follows:

(1) Under S_{pre} conditions, the maximum discrepancy between the experimental and simulation results was 0.1 MPa, with a maximum error of 1%, which is negligible.

(2) After loading S_{in} condition, the finite element analysis predicted a stress result of 115.3 MPa, while the experimental results ranged between 117.64–121.71 MPa, both higher than the finite element analysis result. The error ranged between 2.1% to 5.4%, primarily due to the initial internal pressure being larger than the one used in the finite element analysis.

(3) After loading the S_b condition, the experimental results exceeded those of the finite element analysis, and the error range increased to between 4.3 and 6.6% compared to the S_{pre} and S_{in} conditions. The increase in error was mainly due to two factors: the internal pressure of loading exceeding the design pressure of 34.5 MPa and the slight deformation of the experimental device under the bearing bending moment.

The maximum error between the experimental and finite element analysis results under the combined effect of internal pressure and bending moment loading was 6.6%, which confirmed the accuracy of the finite element analysis, irrespective of the source of the error.

Table 7. Strain gauge location stress results.

Number of Experiments	Working Condition	Strain Gauge Position	Experimental Stress (MPa)	Finite Element Analysis Stress (MPa)	Error (%)
1	S_{pre}	1	0.90	0.91	1
		2	0.90		1
		3	0.91		0
		4	0.91		0
	S_{in}	1	118.69	115.30	2.5
		2	119.16		3.3
		3	120.71		4.6
		4	117.94		2.3
	S_b	1	146.57	139.09	5.4
		2	235.38	221.24	6.4
		3	145.01	139.09	4.3
		4	315.33	297.28	6.1
2	S_{pre}	1	0.91	0.91	0
		2	0.91		0
		3	0.91		0
		4	0.92		1
	S_{in}	1	119.24	115.30	3.4
		2	121.53		5.4
		3	120.60		4.6
		4	120.49		4.5
	S_b	1	147.04	139.09	5.7
		2	235.50	221.24	6.4
		3	148.11	139.09	6.4
		4	317.03	297.28	6.6
3	S_{pre}	1	0.90	0.91	1
		2	0.91		0
		3	090		1
		4	0.92		0
	S_{in}	1	117.98	115.30	2.3
		2	118.63		2.6
		3	117.64		2.1
		4	119.28		3.5
	S_b	1	145.38	139.09	4.5
		2	233.56	221.24	5.6
		3	146.46	139.09	5.3
		4	315.89	297.28	6.3

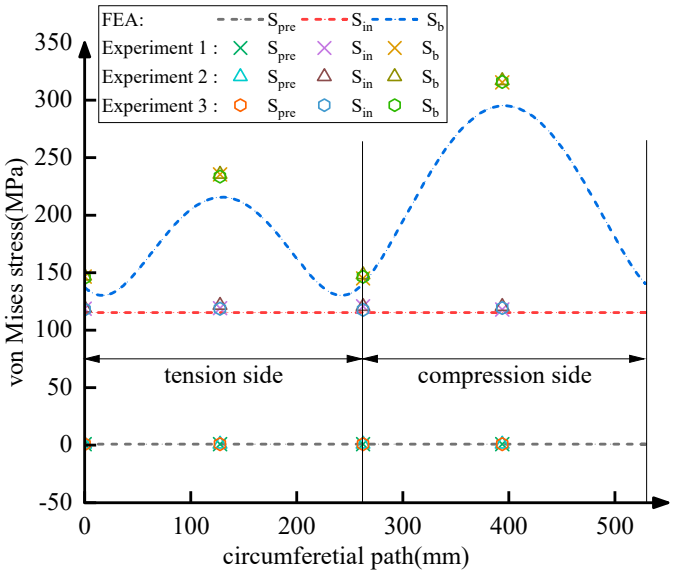

Figure 21. Comparison of experimental stress with simulation.

6. Conclusions

This study presents a theoretical analysis of the intricate load transfer relationship among the subsea clamp connector structures under various working conditions. Finite element simulation is utilized to examine the strength and sealing effectiveness of the key sealing components of six-inch subsea clamp connector subjected to 34.5 MPa internal pressure, 174 kNm bending moment, and axial 212 kN tensile load. Subsequently, an experimental setup was devised to verify the accuracy of the finite element simulation. The primary findings are as follows:

(1) The paper presents a theoretical analysis of the load transfer relationship between the subsea connector components under different working conditions. The analysis considers various factors such as friction between clamp and hub, hub and sealing gasket, and contact angle and diameter. The study establishes a mathematical model between the locking torque and contact pressure under the preloading mode, and proposes the concept of mechanical transfer efficiency. Additionally, a mathematical model of the load transfer between the locking torque and design pressure of the subsea connector is developed based on the sealing criterion under operational mode. The theoretical models provide a basis for the structural design, optimization, and mechanical behavior analysis of subsea connectors.

(2) Simulation results studying the effect of complex load superposition on the mechanical behavior and sealing performance of the core-sealing components of six-inch subsea clamp connector demonstrate the following: (a) The connector will not lead to failure and loss of leak tightness under 34.5 MPa internal pressure, 174 kNm bending moment and 212 kN axial tensile load. (b) After the moment load superposition, the maximum stresses in both the mobile hub and the fixed hub occur on the pressurized side. The contact pressure and width of the contact zone are reduced on both sides of the seal in tension, which greatly impacts the seal. (c) The superposition of axial tensile load will weaken the unevenness of stress distribution caused by the bending moment at the connection of the two hubs, but will further aggravate the unevenness of stress distribution away from the connection of the two hubs. For the metal sealing gasket, this will further reduce the starting contact pressure and contact width, especially for the tensile sides.

(3) An experimental setup was developed to test the strength and sealing performance of the six-inch subsea clamp connector under the influence of 34.5 MPa internal pressure and 174 kNm moment loading and to compare the results with those obtained from finite element analysis. The experimental findings are as follows: (a) The sealing performance was excellent as there was no leakage observed during the experiments, and the maximum pressure drop was only 0.2 MPa in all three trials. (b) The maximum discrepancy between

the critical stress positions of the mobile hub obtained from the experimental and simulation results was 6.4%, indicating good agreement and verifying the accuracy of the simulation.

This paper presents a theoretical mathematical model used as input conditions for finite element simulations and experimental analysis. The experimental results demonstrate the consistency between the theoretical mathematical model and the finite element simulations, which validates the rationality of the theoretical mathematical model. However, direct validation of the theoretical mathematical model and analysis and correction of any resulting errors require further investigation in future work. It is worth noting that when subjected to a large load, plastic deformation occurs near the seal contact surface of the metal sealing gasket, which is confirmed by the simulation results. Thus, the influence of plasticity will be taken into consideration in future research. In future studies, we will consider a more accurate axisymmetric fine mesh model and a more accurate multilinear isotropic hardening model.

Author Contributions: Conceptualization, F.Y. and X.H.; methodology, F.Y., X.H. and L.W.; validation, P.J., X.C. and F.Y.; formal analysis, X.C., K.J. and F.Y.; investigation, F.Y. and X.H.; resources, F.Y. and L.W.; data curation, X.H., L.W. and X.W.; writing—original draft preparation, L.W., X.W. and F.Y.; writing—review and editing, P.J., K.J. and X.H.; funding acquisition, F.Y. All authors have read and agreed to the published version of the manuscript.

Funding: This research was funded by the National Natural Science Foundation Of China, grant number 52001089; Heilongjiang Provincial Natural Science Foundation Of China, grant number LH2021E046; and National Natural Science Foundation of China, grant number 52001116.

Institutional Review Board Statement: Not applicable.

Informed Consent Statement: Not applicable.

Data Availability Statement: Data sharing not applicable.

Conflicts of Interest: The authors declare no conflict of interest.

References

1. Wu, J.-H.; Zhen, X.-W.; Liu, G.; Huang, Y. Optimization design on the riser system of next generation subsea production system with the assistance of DOE and surrogate model techniques. *Appl. Ocean Res.* **2019**, *85*, 34–44. [CrossRef]
2. Vedachalam, N.; Srinivasalu, S.; Ramesh, R.; Aarthi, A.; Ramadass, G.; Atmanand, M. Review and reliability modeling of maturing subsea hydrocarbon boosting systems. *J. Nat. Gas Sci. Eng.* **2015**, *25*, 284–296. [CrossRef]
3. Cascales, D.H.; Militello, C. An accurate simple model to evaluate integral flange rotation. *Int. J. Press. Vessels Pip.* **1987**, *30*, 151–159. [CrossRef]
4. Dekker, C.J.; Stikvoort, W.J. Improved design rules for pipe clamp connectors. *Int. J. Press. Vessels Pip.* **2004**, *81*, 141–157.
5. Abid, M.; Chattha, J.A.; Khan, K.A. Finite element analysis of a gasketed flange joint under combined internal pressure and thermal transient loading. In Proceedings of the ASME Pressure Vessels and Piping Conference, San Antonio, TX, USA, 22–26 July 2007; pp. 261–267.
6. Krishna, M.M.; Shunmugam, M.; Prasad, N.S. A study on the sealing performance of bolted flange joints with gaskets using finite element analysis. *Int. J. Press. Vessels Pip.* **2007**, *84*, 349–357. [CrossRef]
7. Takagi, Y.; Torii, H.; Omiya, Y.; Kobayash, T.; Sawa, T. FEM Stress Analysis and the Sealing Performance Prediction of Pipe Flange Connections under External Bending Moments and Internal Pressure. *J. Solid Mech. Mater. Eng.* **2013**, *7*, 486–495. [CrossRef]
8. Wang, Y.; Zong, L.; Shi, Y. Bending behavior and design model of bolted flange-plate connection. *J. Constr. Steel Res.* **2013**, *84*, 1–16. [CrossRef]
9. Abid, M.; Awan, A.W.; Nash, D.H. Determination of load capacity of a non-gasketed flange joint under combined internal pressure, axial and bending loading for safe strength and sealing. *J. Braz. Soc. Mech. Sci. Eng.* **2014**, *36*, 477–490. [CrossRef]
10. Peng, F.; Duan, M.; Wang, J.; Zhu, Y.; Wang, X. Optimisation method for mathematical model of deepwater collet connector locking mechanism. *Ships Offshore Struct.* **2015**, *11*, 575–590. [CrossRef]
11. Nelson, N.R.; Prasad, N.S. Sealing behavior of twin gasketed flange joints. *Int. J. Press. Vessels Pip.* **2016**, *138*, 45–50.
12. Yun, F.; Wang, L.; Yao, S.; Liu, J.; Liu, T.; Wang, R. Analytical and experimental study on sealing contact characteristics of subsea collet connectors. *Adv. Mech. Eng.* **2017**, *9*, 1–14. [CrossRef]
13. Zhang, K.; Huang, H.; Duan, M.; Hong, Y.; Estefen, S.F. Theoretical investigation of the compression limits of sealing structures in complex load transferring between subsea connector components. *J. Nat. Gas Sci. Eng.* **2017**, *44*, 202–213. [CrossRef]
14. Chen, W.; Di, Q.; Zhang, H.; Chen, F.; Wang, W. The sealing mechanism of tubing and casing premium threaded connections under complex loads. *J. Pet. Sci. Eng.* **2018**, *171*, 724–730. [CrossRef]

15. Wang, L.-Q.; Wei, Z.-L.; Yao, S.-M.; Guan, Y.; Li, S.-K. Sealing Performance and Optimization of a Subsea Pipeline Mechanical Connector. *Chin. J. Mech. Eng.* **2018**, *31*, 18. [CrossRef]
16. Li, Y.; Zhao, H.; Wang, D.; Xu, Y. Metal sealing mechanism and experimental study of the subsea wellhead connector. *J. Braz. Soc. Mech. Sci. Eng.* **2019**, *42*, 26.
17. Liu, X.-C.; Cui, F.-Y.; Jiang, Z.-Q.; Wang, X.-Q.; Xu, L.; Shang, Z.-X.; Cui, X.-X. Tension–bend–shear capacity of bolted-flange connection for square steel tube column. *Eng. Struct.* **2019**, *201*, 109798.
18. Liu, M.; Zhang, L.; Wang, L.; Liu, H.; Sun, Y.; Wang, Y. The leakage analysis of submarine pipeline connecter based on a new fractal porous media model. *Desalin. Water Treat.* **2020**, *188*, 390–399. [CrossRef]
19. Duan, M.; Zhang, K.; Soares, C.G.; Paik, J.K. Theoretical investigation on hub structure design of subsea connectors. *Thin-Walled Struct.* **2020**, *159*, 107036. [CrossRef]
20. Li, Y.; Su, H.; Wang, Y.; Mou, L.; Wang, Q.; Ren, Y. Research on bearing capacity and sealing contact characteristics of the subsea wellhead connector. *Proc. Inst. Mech. Eng. Part M J. Eng. Marit. Environ.* **2022**, *237*, 153–165. [CrossRef]
21. Yun, F.; Liu, D.; Xu, X.; Jiao, K.; Hao, X.; Wang, L.; Yan, Z.; Jia, P.; Wang, X.; Liang, B. Thermal–Structural Coupling Analysis of Subsea Connector Sealing Contact. *Appl. Sci.* **2022**, *12*, 3194. [CrossRef]
22. Zhang, K.; Cheng, H.; Liu, J.; Wang, H. Analytical calculation method for predicting contact loads and structural strength of metallic gasket of subsea connectors under thermal loads. *Proc. Inst. Mech. Eng. Part M J. Eng. Marit. Environ.* **2023**. [CrossRef]
23. Li, Y.; Su, H.; Jiang, W.; Cai, Z.; Chen, J. Sealing performance of subsea wellhead connector under thermal-structural coupling. *Ocean Eng.* **2023**, *270*, 113504. [CrossRef]
24. Zhao, H.; Chen, R.; Luo, X.; Duan, M.; Lu, Y.; Fu, G.; Tian, H.; Ye, D. Metal sealing performance of subsea X-tree wellhead connector sealer. *Chin. J. Mech. Eng.* **2015**, *28*, 649–656. [CrossRef]
25. Yun, F.; Wang, G.; Yan, Z.; Jia, P.; Xu, X.; Wang, L.; Sun, H.; Liu, W. Analysis of Sealing and Leakage Performance of the Subsea Collet Connector with Lens-Type Sealing Structure. *J. Mar. Sci. Eng.* **2020**, *8*, 444. [CrossRef]
26. Murtagian, G.R.; Fanelli, V.; Villasante, J.A.; Johnson, D.H.; Ernst, H.A. Sealability of Stationary Metal-to-Metal Seals. *J. Tribol.* **2004**, *126*, 591–596. [CrossRef]
27. Horgan, C.O. Recent Developments Concerning Saint-Venant's Principle: An Update. *Appl. Mech. Rev.* **1989**, *42*, 295–303. [CrossRef]
28. *A.S. 6A*; Specification for Wellhead and Tree Equipment. American Petroleum Institute: Washington, DC, USA, 2018.